

Predicting and Evaluating the Performance of Sparse Permanent Array Networks for Microseismic Monitoring

Elige B. Grant¹, Paul A. Nyffenegger^{1,2}, and Kevin D. Hutchenson^{1,2}, ¹Quantum Technology Sciences, Inc. (Quantum); ²Geospace Technologies, Inc

Summary

Microseismic monitoring results are currently used as a measure of the state of underground assets to inform ongoing operations and as a risk management strategy. In November 2021, four permanent compact volumetric phased arrays (SADAR arrays) were installed at Carbon Management Canada's Newell County Field Research Station (FRS) for monitoring CO₂ sequestration (Nyffenegger *et al.*, 2022; Zhang *et al.*, 2023; Hutchenson *et al.*, 2023). A previous effort developed a performance model for microseismic detection based on a systems engineering approach including a signal detection framework (Nyffenegger *et al.*, 2023). This work extends the previous publication by including the model for source level terms and the algorithmic implementation, and then discusses the computed performance prediction.

We assess the effectiveness of the sparse network of SADAR arrays for microseismic monitoring using this performance prediction along with validation data drawn from the microseismic bulletin for the FRS. In short, effectiveness of the sparse network is predicted by estimating the magnitude of completeness (Mc) for locatable events occurring within the monitored volume. The model is then validated using the location, depth, and magnitude parameters from the network event bulletin. The model validation is ongoing and periodically updated as the bulletin is updated.

This performance model and implementation are transportable to other production, gas storage, disposal, and mining operations via input of local measurements, conditions, and configurations. An accurate understanding of a microseismic monitoring system performance can be generated when including local noise measurements, state of stress, and earth model properties. The model, therefore, has application as a planning tool, and for confirming that the network and processing system is performing as expected using a local event bulletin.

Introduction

Developing underground assets for resource production, waste disposal, or heat extraction represent a considerable investment. Prior to expending funds, risk analysis is undertaken to determine what kinds of liabilities may occur, probabilities of any being realized, and the severity of the consequences on operations. Induced seismicity is an obvious and significant risk to any operations centered on underground assets because of potential damage to the industrial infrastructure and the geological assets themselves. Additionally, perceived hazards by the public, liability jeopardy from unwarranted litigation, and regulatory responses are non-negligible factors.

Examples of induced seismicity are not new or rare. Induced seismicity has been reported linked to underground mining, solution mining, geothermal energy production, and large hydroelectric projects. Many publications exist reporting induced seismicity within oil and gas regions in

conjunction with production, engineering, and disposal wells (e.g., Buchanan *et al.*, 2023). Recently, significant induced seismicity has been reported associated with a few geologic carbon storage (GCS) projects; for example, the In-Salah project (Stork *et al.*, 2015) and the Illinois Basin-Decatur project (Dichiarante *et al.*, 2021; Bauer *et al.*, 2022). Any induced seismicity that results in additional engineering, operations changes, or financial outlay we define as significant from the field/facilities operator's or regulator's view.

Measurement, monitoring, and verification (MMV) systems for these enterprises are important for understanding the state of the local underground geologic structures because the subsurface is never completely known or predictable. Operators, regulating agencies, and liability insurers desire seismicity monitoring to ensure safety of personnel, infrastructure, equipment, and geological assets. Microseismic monitoring measures the response of the geology to production, storage, and mining activities that may be used to inform operations. For example, microseismic monitoring in mining identifies safety risks that could be ahead of equipment (e.g., shearer) or behind (e.g., methane) or indicate instability developing in room and pillar systems. In geothermal energy production, microseismic monitoring helps measure changes of state in fluid/heat exchange zones, or, in steam assisted ultra-heavy oil production, indicates changes in steam chambers potentially warning of structural instability. Monitoring and measurements indicating when the state of the geologic assets change in a way that pushes a risk toward becoming an issue is a technical approach to managing these risks.

Microseismic monitoring systems traditionally use networks of surface sensors and/or downhole sensor strings for detecting and locating seismicity ranging from microseismic-to-felt event magnitudes (Eaton, 2018, 136). These networks usually cover a wide area using single vertical or multi-component geophone stations installed in post-holes or in shallow vaults across the area of review. Alternately, some monitoring programs focus on deploying a string of instruments in boreholes. The advantages of deploying local instruments compared to relying on regional networks are the ability to use less expensive geophones versus broadband sensors, detection and location of microseismic events within the area of review, more precise location and depth solutions, and ability to produce a bulletin of local events with a magnitudes of completeness below felt-event thresholds (e.g. Roux *et al.*, 2014; Fang *et al.*, 2024). Disadvantages include having to mitigate local industrial noise fields, installing and sustaining a substantial sensor network distributed over the area of review, or, for borehole monitoring systems, drilling and instrumenting additional boreholes which introduces other technical risks, and of course, managing and processing all the acquired data. Also, not all surface areas required for a uniform network coverage may be accessible based on landowner preferences, power and communications infrastructure, or local regulations, so maintaining the flexibility or agility of these traditional systems while ensuring they meet the technical requirements may be difficult.

Emplacing a sparse network of compact volumetric phased arrays (SADAR arrays) permanently installed in shallow boreholes is a modern approach that provides predictable and robust performance for the long haul while having immediate advantages in reduced infrastructure, sensor population, and surface site footprint compared with equivalent surface systems.

Technical advantages using the SADAR arrays include an immediately lower noise level due to depth away from the surface but also capabilities only provided by these phased arrays, including 1) coherently processing the data via beamforming immediately creating a gain; 2) unambiguously resolving the signal angle of arrival; 3) independently measuring phase velocity of the signal across the array, and 4) ability of separating signals of interest and clutter signals arriving simultaneously along different direction. Furthermore, a sparse network of SADAR arrays allows immediately excluding signals from events occurring outside of the area of review, producing a local seismicity bulletin with a magnitude of completeness below felt-event thresholds, and long term stability of performance and event reporting capabilities owing to the SADAR arrays tolerance of sensor attrition (Quigley *et al.*, 2025; Hutchenson *et al.*, 2025). In addition, the SADAR arrays provide dual-use for passive monitoring and active-source imaging (Nyffenegger *et al.*, 2025; Quigley *et al.*, 2025).

A previous effort developed a performance model for microseismic detection based on a systems engineering approach including a signal detection framework (Nyffenegger *et al.*, 2023b). This work extends the analysis by including the model for source level terms and the algorithmic implementation. Results of the performance prediction are discussed in terms of abilities of the SADAR network to detect, locate, and determine the moment magnitude M_w of events within the monitored volume; the overall M_c for locatable events occurring within the monitored volume is estimated from the model results. The performance model prediction serves as a valuable planning tool, providing essential information needed for MMV plans and development efforts.

The monitoring effectiveness of the network is then assessed using this performance prediction compared with the validation data accumulated in the FRS microseismic bulletin. The analyst-vetted microseismic bulletin from the array network includes event time, location, depth, and moment magnitude, providing a realistic view of where the data confirms model results and where there is no support due to lack of validation data.

Background

The Containment and Monitoring Institute of Carbon Management Canada operates the Newell County FRS in Southern Alberta (Figure 1), a GCS pilot site for evaluating technologies (Lawton *et al.*, 2019; Macquet *et al.*, 2019). The operations at the FRS support development, testing, and demonstrating operational effectiveness of MMV tools for minimizing risks associated with GCS, using small volumes of CO_2 injected into the Basal Belly River Sandstone (BBRS, $z=300\text{m}$) (Macquet *et al.*, 2022).

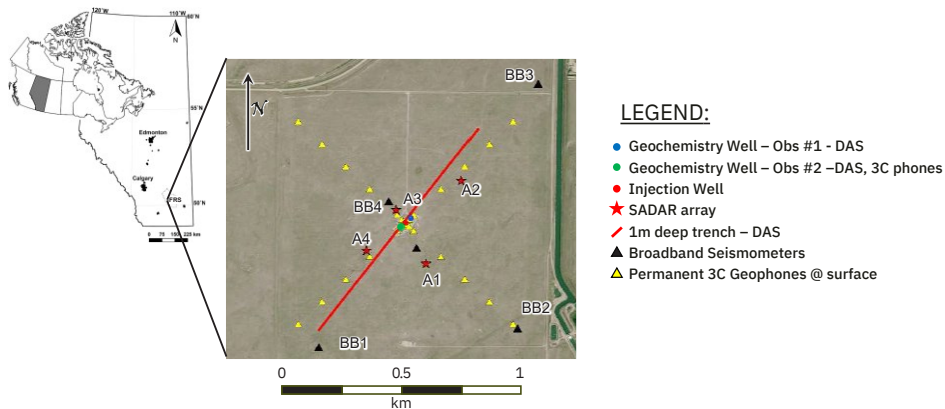


Figure 1. Location of the Carbon Management Canada Newell County Field Research Station, Alberta, Canada. The zoomed view indicates the injection well (red square) and the four SADAR arrays (stars), and other deployed seismic equipment. SADAR array A3 is 70 m northwest of the injection well, arrays A1 and A4 are 200 m from the injection well, array A2 is 300 m northeast of the well.

In November 2021, Quantum Technology Sciences (Quantum) installed a sparse network of four dual-use permanent SADAR arrays at the site to demonstrate their utility for MMV at an active GCS facility (Nyffenegger *et al.*, 2025; Nyffenegger *et al.*, 2023a; Zhang *et al.*, 2023; Hutchenson *et al.*, 2023). Details about phased array design goals and considerations were discussed in Nyffenegger *et al.*, 2023b. Nevertheless, design is always a site-specific exercise in understanding the tradeoffs between signal coherency limits, correlation and directionality of the noise and clutter fields, and the array gain and directivity required to maximize the signal signal-to-noise ratio (SNR) within the desired frequency band. Combined with an understanding of the geophysical properties local to where the site, the primary design goal for a phased array can be stated as creating the largest aperture warranted under the coherence length, using the array element separation supported by the noise correlation distance, for suppressing the site noise and clutter signals given the required design frequencies and bandwidth.

The arrays and network were designed for microseismic monitoring of the BBRS reservoir with a seismic event detection monitoring requirement down to a magnitude of -3 Mw and Mc of -2 Mw, for alerting to possible confinement failure within the caprock or the reservoir itself. The four arrays installed at the FRS are based on uniform cylindrical array (UCA) geometries with diameters ranging from 4m to 7.5m (Figures 2 and 3) and are designed to provide testable configurations. The “standard” design, configured as an octagon with a central axis and with six uniformly spaced levels vertically, is deployed for arrays A1 and A2. The “wide aperture” layout, consists of nested UCAs with a larger radius with the outermost decagon and an inner hexagon layout, and three uniformly spaced levels, is used for array A3. Array A4, is configured as a “Hybrid” of the standard and wide aperture designs with the inner hexagon UCA having six levels. All array elements consist of vertical 10 Hz geophones installed and grouted in shallow boreholes between 9m-19m depth below the weathering zone. Since installation the system has been operating at 98.7% availability with no down time for maintenance.

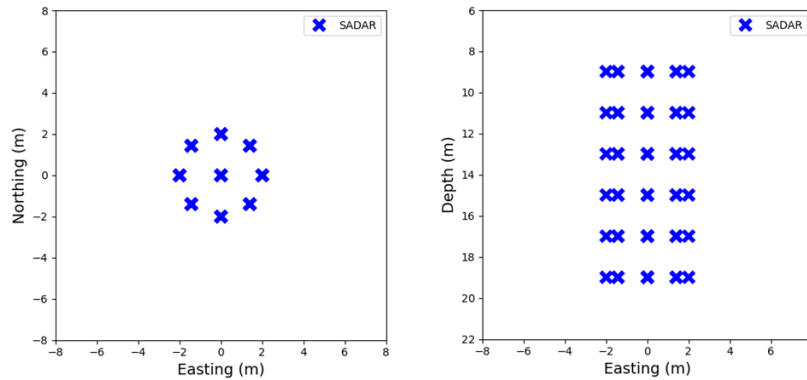


Figure 2. Array design “standard” shown at left in map view and right in profile view.

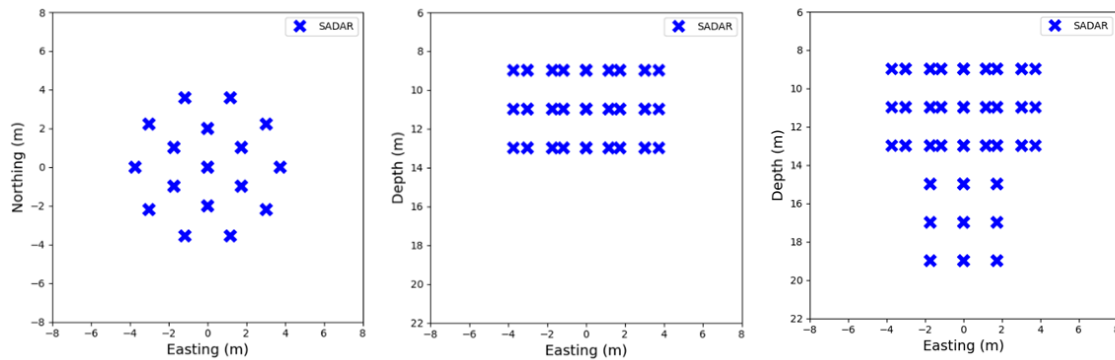


Figure 3. Array designs “wide aperture” shown at left in map view and center in profile view, and “hybrid” profile view shown at right.

For any of these systems, justifying initial capital expenses while ensuring long-term performance warrants a model-based approach. Monitoring system requirements, geological structure and associated geophysical properties, and land use restrictions become critical inputs. The output, the monitoring system performance prediction, consists of the lowest magnitude event detectable as a function of absolute location per array, followed by incorporating SNR-like thresholds allowing a prediction of the magnitude of completeness M_c for locatable events across the network. Validating the model using collected signals and the associated computed event locations and magnitudes is essential for building confidence in the monitoring system.

Theory

The underlying mathematical basis for understanding and evaluating SADAR system performance based on the sonar equation approach is explained in Nyffenegger *et al.*, 2023b. That paper included measurements to further the understanding of several of the terms of the performance equations, but did not include computation of the predicted network performance

across the area of review or validation of the model predictions. This work extends that effort by including source level models, the algorithm, and results for the computation of the performance prediction. Portions of the system analysis critical to understanding the performance model results are restated here and follow system analysis as given in Urick (1983), Burdic (1991), Ainslie (2010), and Abraham (2019), as well as having some common elements with Boatwright and Choy (1986), Choy *et al.*, (2001), and Boatwright *et al.*, (2002).

The received signal is considered from the perspective of a single element (or receiver) located at a fixed point (x, y, z) , receiving a field containing a mixture of the signal of interest and competing clutter signals as well as a variety of noise processes. The element exists in an engineered phased array of like elements with identical responses. Let:

$S(x, t, f)$ represents a signal of interest (SOI) received by the array elements, embedded in the series of continuously acquired data,

$\alpha(t, f, \phi, \theta)$ is a beamformed series derived using the acquired data from all elements, and

(ϕ, θ) is the angle of arrival broken into azimuth ϕ and depression angle θ , defined as the vector pointing outward from the array centroid

Assuming plane waves, signals arriving at array elements along angle (ϕ, θ) with a specific phase velocity are combined to emphasize the coherent SOI and suppress clutter and noise, resulting in the beamed series represented as $\alpha(t, f)$. Angle (ϕ, θ) along with phase velocity then define the beam main response axis (MRA), and $\alpha(t, f)$ is specific to the beam and MRA.

Following a signal detection paradigm, the problem becomes identifying $S(x, t, f)$ and extracting characteristics and information pertinent to $S(x, t, f)$ from the derived series $\alpha(t, f)$ in the presence of competing and interfering unknown noise. Some measure of the presence of the signal derived from $\alpha(t, f)$ is required to detect the SOI, and then that measure must surpass a minimum threshold to achieve a required probability-of-detection. For example, the common “energy detector” approach includes forming a metric in terms of SNR power (\mathcal{S}) as a function of frequency derived from the short-term average power written as $|\alpha(t, f)|$:

$$E[\mathcal{S}] = \frac{|\alpha(t, f)|}{E[\text{noise}(\alpha(t, f))]} \geq \text{threshold} \quad (1)$$

where $E[\cdot]$ is the expectation operator. The denominator represents the statistical estimate of the noise power in the series $\alpha(t, f)$, and recognize the signal component in the numerator is contaminated by the instantaneous noise. The expected SNR ($E(\mathcal{S})$) from equation (1) can be partitioned as independent factors on the right-hand side corresponding to system components and operations, where signal gains appear in the numerator and signal losses are in the denominator, and where frequency dependence is implicit in each factor. Equation (1) written into decibels becomes:

$$10 \log_{10}[E(\mathcal{S})] \geq 10 \log_{10}(\text{threshold}) \text{ dB re: power} \quad (2)$$

where the left-hand side is in units of decibels of the power and the right-hand side, hereafter written as DT is the detection threshold in decibels. Substituting for $E(S)$ and writing the SNR power as partitioned factors yields:

$$DT \leq (SL - RP) - PL - (NL_f - AG - SP) + PG \quad . \quad (3)$$

where:

- SL is the source level;
- RP is the radiation pattern of the source;
- PL is the propagation loss, a compound term;
- NL_f is the noise spectrum level, a compound term;
- AG is the array gain (if phased arrays are deployed);
- SP is the sensitivity pattern of the sensor element itself; and
- PG is gain due to signal processing, post beamforming if arrays are deployed.

Defining signal excess (SE) as the portion of the SNR power greater than the detection threshold, equation (3) becomes

$$SE = [(SL - RP) - PL - (NL_f - (AG + SP)) + PG] - DT \quad . \quad (4)$$

The received signal level is the portion of equation (4) that describes the physical signal measured at any individual sensor, neglecting instantaneous noise, and prior to array and processing gains:

$$received\ signal = [(SL - RP) - PL + SP]. \quad (5)$$

Equation (4) parameterizes the trade-off space of independent factors that describe the potential of the system to detect the SOI, *i.e.*, a model of the system performance. As SE drops below 0 dB, the potential of a system for both detecting and locating a seismic event will also vanish.

The terms in equation (4) can be addressed individually as a function of source position and receiver position and configuration. Neglecting sensitivity pattern (SP), six main degrees of freedom are identified (lumping RP together with SL). The source level (SL), propagation loss (PL), and noise level (NL_f) are the three main uncontrolled factors depending on the physical system independent of sensing and data acquisition. The array gain (AG), other processing gain (PG), and the detection threshold (DT) factors represent the processing system components that can be controlled to affect the signal excess SE and register a signal detection.

Nyffenegger *et al.* (2023b) discusses array gain, estimating the propagation loss factor, and considerations regarding noise, noise components, and noise measurement; those discussions are not repeated here. However, the previous effort did not address source level modeling inputs to performance prediction. The required inputs for estimating the source level (SL) are the earth model properties (V_p , V_s , ρ), the moment magnitude (M_w), and the stress drop ($\Delta\sigma$) in units of Pascals. The goal is to define the frequency dependent displacement source level referenced to a fiducial distance from the event origin separate from the whole path propagation loss. Let:

Ψ_0 represent the spectral zero-frequency displacement amplitude at the fiducial distance, and f_c be the spectral corner frequency.

After Brune (1970, 1971), the source level (SL) in decibels becomes:

$$SL = 20 \log_{10} \frac{\Psi_0}{1 + \left(\frac{f}{f_c}\right)^2} \quad (6)$$

To find Ψ_0 , first determine the seismic moment (M_0) in units of N-m from the moment magnitude:

$$M_0 = \frac{10^{\frac{3}{2}M_w + 16.1}}{10^7} \quad (7)$$

The spectral zero-frequency displacement amplitude (Ψ_0) is then:

$$\Psi_0 = \frac{M_0}{4\pi\rho\nu^3} \quad (8)$$

where,

- ρ is the density (kg/m^3),
- ν is the P-wave velocity (α) or S-wave velocity (β) in (m/s), and
- Ψ_0 is the Brune zero-frequency displacement amplitude (Ω_0) without accounting for geometrical spreading.

To find f_c , determine the radius (r) of a circular fault in units of meters, using:

$$r = \sqrt[3]{\frac{7M_0}{16\Delta\sigma}} \quad (9)$$

after Keilis-Borok (1959). The event spectral corner frequency is then:

$$f_c = \left(\frac{\beta}{2\pi r}\right)^2 \sqrt{\frac{7\pi}{4}} \quad (10)$$

where β is the shear-wave velocity at the source location, after Brune (1970, 1971).

Focal mechanisms are assumed to be unknown for this study, so the radiation pattern ($\mathcal{R}_{\theta\varphi}$) accounts for the fractional amount of the total possible energy that radiates in a specific direction from the source. Following Aki and Richards (2002, pg. 115) the average P- or S-wave radiation pattern ($\langle \mathcal{R}_{\theta\varphi} \rangle$) is set equal to the root-mean-squared value:

- $\langle \mathcal{R}_{\theta\varphi} \rangle = 2/\sqrt{15}$ P-wave, and
- $\langle \mathcal{R}_{\theta\varphi} \rangle = \sqrt{(2/5)}$ S-wave,

and the radiation pattern term (RP) in decibels becomes:

$$RP = 20 \log_{10} \frac{1}{\langle \mathcal{R}_{\theta\varphi} \rangle} \quad (11)$$

Workflow and Results

Performance models predict the minimum Mw magnitude event detectable and locatable by the monitoring network and data processing system across the monitored volume. The equation (4) inputs are the measured surface noise levels, modeled source levels, earth properties model,

array and processing gains, and threshold. We estimate SE from equation (4) as a function of the other terms considering the six degrees of freedom, over the frequency band 10 Hz – 300 Hz determined from the observed event and noise spectra. Because propagation loss (PL) estimates must be computed as a function of position, a 3D grid having 5x5x5m cells is defined to represent the monitored volume at the FRS, each grid cell representing a hypothetical source location (see Nyffenegger *et al.*, 2023b). To estimate the total signal propagation loss (PL), we perform ray tracing between each grid cell and the array location. Currently, only a 1D earth properties model is used, but the ray tracing algorithm allows the assignment of properties for the grid cells independently.

Noise level (NL_f) expected values are measured independently for each array. Starting with one minute duration noise buffers, power spectra were computed for 0.5 second frames drawn from the noise buffer with a Hann window applied to each frame, and frames overlapped by 50%. An averaged power spectra is output. Noise levels may be compared across hours and days or with surface sensor networks whenever emplacements are co-located, as shown in Figure 4 and Figure 5 for example. The planar surface array shown in Figure 4 consists of 51 Geospace GCL 3C nodal units with 10 Hz geophones with the inner 17 nodes arranged on top of the A3 borehole locations. The design incorporates the inner 17 into nested uniform circular arrays having a maximum horizontal aperture of ~24m, and multiple design frequencies between ~70 Hz and ~200 Hz assuming an in-plane incident compressional wave.

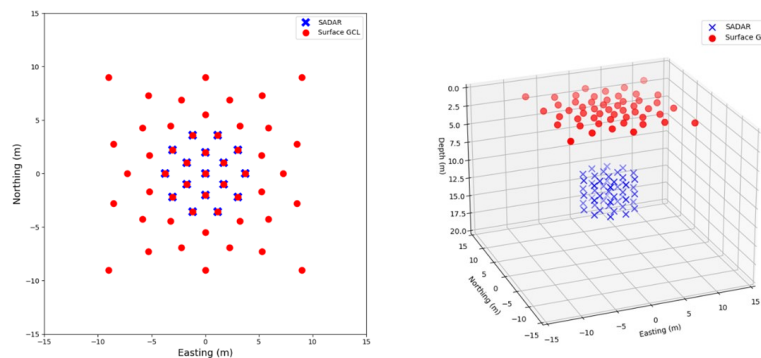


Figure 4. Array A3 (wide-aperture design) and the temporary surface array of 51 nodal units, shown at left in map view and right in a three-dimensional view.

The noise level (NL_f) comparison shown in Figure 5 between the surface layout (red) and SADAR array A3 (black) demonstrates the initial gain for locating sensors at ~10m and deeper. For single sensors, the gain from at depth emplacement is a minimum of 2 dB at long wavelengths, reaching ~24 dB at higher frequencies of observed signals (~125 Hz) depending on time of day. For the bulk of the frequency band typical of signals observed at the NCF (30 to 90 Hz), the gain is ~12 dB or better from emplacement at-depth alone.

The spectra for the individual channels indicate the overnight noise levels below ~40 Hz are dominated by ambient environmental noise, whereas system noise levels dominate over the flat part of the spectral estimate at greater frequencies. Compared with mid-day noise levels, the ambient/system noise corner is observed greater than 100 Hz for the SADAR array single channels and is not clear for single channels from the surface deployment.

Estimates of array gain (AG) across the total variety of beams, technically a measured quantity, is difficult to generalize. Zhang *et al.*, (2023) provides some individual measured values comparing single sensors in the array and on the surface. For performance prediction, AG is approximated using incoherent stacks of noise records per array as shown in the Figure 5 example (dashed lines). For an array of N elements, we expect a minimum reduction in random noise of $10 \log_{10} N$ decibels from theoretical considerations (Urick, 1983), and not considering the spatial filtering gain from the array directional response, corresponding to ~17 dB to ~19 dB.

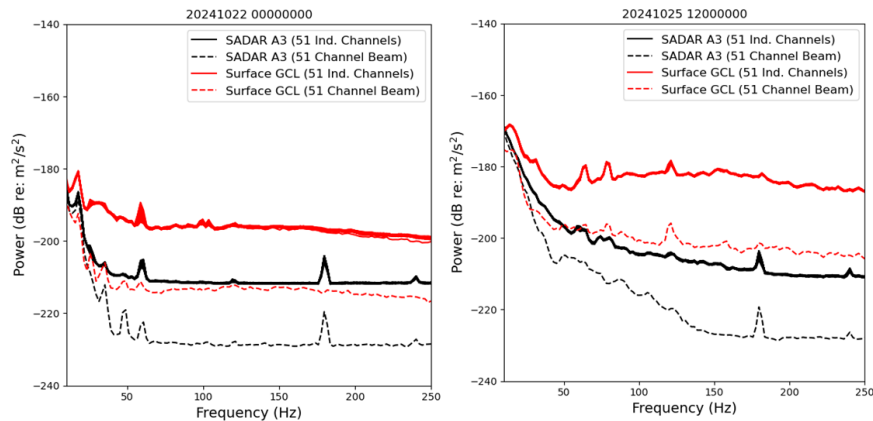


Figure 5. Example noise levels for vertical geophones emplaced at A3 on the surface (red) and for the permanent SADAR array (black), measured for the overnight (left) and mid-day (right) periods.

The spectral estimates shown in Figure 5 support the theoretical estimates as the minimum AG . In addition, the stack suppresses the system noise such that the ambient/system noise corner is shifted to ~70 Hz in the overnight estimate and ~150 Hz in the mid-day estimate. In-beam AG case-by-case measurements will improve over these values within the designed frequency band.

The spectral level (NL_f) in the band below 30Hz is dominated by more coherent ambient seismic noise and clutter signals inferred from the reduced AG values. This band is at least a factor of 3 below the lowest array design frequency so we would not expect significant noise suppression from an incoherent sum because at corresponding wavelengths the noise on the separate channels should not be independent. In other words, the element spacing for both the SADAR and the surface arrays is smaller than the noise correlation distance.

Source level model (SL) from equation (6) is calculated for a magnitude range of -3 Mw to -1 Mw, a very low stress drop of 1 kPa, and attenuation $Q = 10$. These factors are derived from

measurements at this site of observed signal power (as a function of frequency) and propagation distance for a subset of located events. However, for general performance predictions the inputs may be estimated from regional studies if no local measurements exist.

Combining the measured and modeled terms then, the theoretical signal excess (SE) is calculated for a variety of source levels (SL) and the smallest SL that results in a positive SE for each grid location and each array is stored. Event detection is important, but events must be locatable, a condition enforced by requiring all 4 arrays (for the FRS network) detect the signal for single phases (*i.e.*, P or S). In cases where combinations of P and S phases are detected, only 3 arrays are required. The angular diversity of distances/azimuths between the detecting arrays is also important and is used to limit the lateral extent where accurate locations are possible. In other words, the network geometry is required to provide the angular coverage that ensures convergence of location algorithms. For this effort, only P phases are used, so the requirement is that all 4 arrays detect the events with a set modeled signal excess (SE) threshold, immediately meeting source-receiver geometry restrictions.

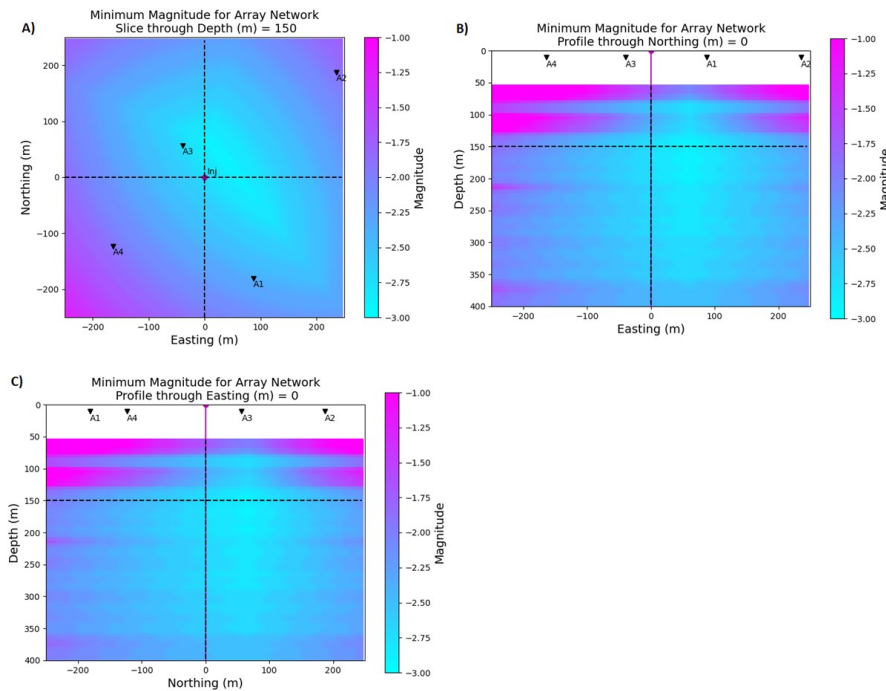


Figure 6. Predicted minimum moment magnitude M_w for cross-sections through the monitored volume at the injection well (labelled with a red diamond or labelled "Inj") for A) horizontal slice through 150m Depth, B) vertical profile through 0m Northing, and C) vertical profile through 0m Easting.

Cross-sections through the performance prediction results for the monitored volume are displayed in Figure 6. The minimum M_w locatable event is modelled by attaining an SE value of 0 dB. The estimated minimum M_w locatable event does not fall to the lowest magnitude tested (-3 Mw)

across the monitored volume. For the horizontal cross-section in Figure 6-A the minimum magnitude detectable approaches the model minimum only near the injection well close to the middle of the network (the trivial result).

The performance model predicts the SADAR sparse network is effective down to -2.5 Mw across the active BBRS reservoir within 65 m to 165 m of the injection well (Figure 6 vertical profiles B, C). Coverage for more shallow horizons (e.g., 100m), geologic units below the BBRS reservoir, and at the extremes of the network is not as sensitive or uniform for the smallest microseismic events, and we suggest these model observations are a common result for most of the published seismic MMV deployments. We suggest for some of the geologic horizons below the BBRS reservoir or along the edges of the network but still within the modeled volume, the performance prediction indicates that -2.0 Mw is a more conservative prediction for the effectiveness of the monitoring network. The prediction result also indicates that as the plume radius expands beyond 100m the network will need to be augmented by at least one array in the northwest quadrant, and as the plume approaches a 200 m radius the network will need to be expanded to provide the existing performance capabilities over a larger area. However, expansion may not need to be uniform and will depend on measured plume dimensions.

For model validation, we produced maps comparable to the performance prediction based on the analyst reviewed FRS bulletin between November 2021 and through October 2024 (Hutchenson *et al.*, 2025; 2023). There were many surface and shallow events ($z \leq 15$ m); including these events, the bulletin contains nearly 10,000 events with magnitudes range between -0.5 to -2.75 Mw. Excluding events with less than 50 m depth, the total number of events considered from the current bulletin is approximately 3350 events. The 3D grid was subdivided into 25x25x25m cells and the minimum magnitude event with location inside each bin/cell was recorded. A final 3x3x3 average cell smoothing operator was applied to only those cells containing information. The resulting validation map (Figure 7) indicates the estimated minimum observed magnitudes located at the specified depth slice/cross-section locations (+/- 1 cell).

The overall agreement using just a visual comparison is good enough to accept the model as is, considering the low seismicity level throughout the region. Some mismatch due to location uncertainty, higher-than-modeled noise levels, and issues in the modeling of travel-times for near-surface events, leading to non-uniqueness and depth mis-location, is expected. The areas in white indicate that there is no validation data support for the model of those cells. No effort to quantify statistical significance of each validation block was performed for this demonstration. Model validation is periodically repeated with the total number of events augmented from the updated bulletin.

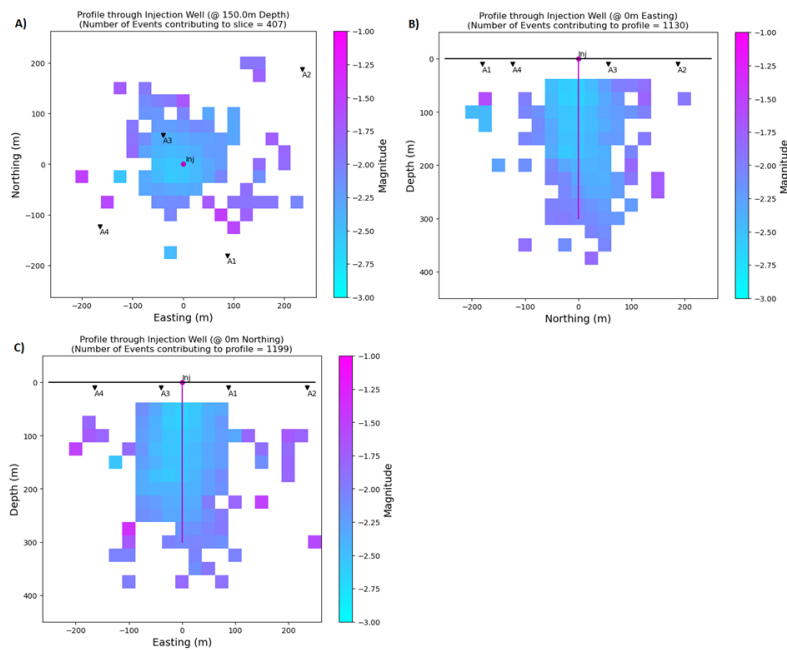


Figure 7. Composite figure showing 3 slices through the current validation set minimum magnitude sort at the injection well A) slice through 150m Depth, B) profile through 0m Northing, and C) profile through 0m Easting.

This validation set can also be used to verify the sparse network is acting as expected in terms of overall detection ranges and received signal power for locatable events. Received signal power is as defined in the equation (5) model, but neglecting radiation and sensitivity pattern terms. Figure 8 shows the measured received signal power averaged across the array versus source-receiver range for 412 reviewed, well-located events occurring over the period November 2021 through October 2023, filtered for depth $z > 10\text{m}$. Each event yields one measurement per array for a total of 1648 measurements, but they cannot be considered as completely independent.

Theoretical received signal power versus range curves are plotted overlaying the Figure 8 scatter plot, assuming constant earth model properties consistent with those at the BBRS reservoir depth and constant stress drop levels, with the only variables being the event magnitude and the distance (*i.e.*, range) between the source and the individual arrays. Also plotted are the measured average individual channel noise power levels for all SADAR arrays (red dashed line) and then the approximate values for noise levels taking into account the gain measured in the optimal beam for $\sim 10\text{ dB}$ minimum gain to $\sim 18\text{ dB}$ maximum expected gain over a single channel (green dashed line and dot-dash line respectively). The difference between the noise plotted in Figure 8 versus Figure 5 is that the former is measured of the mean power in the time domain across the band of interest, whereas the latter is a measure of the power at individual frequencies.

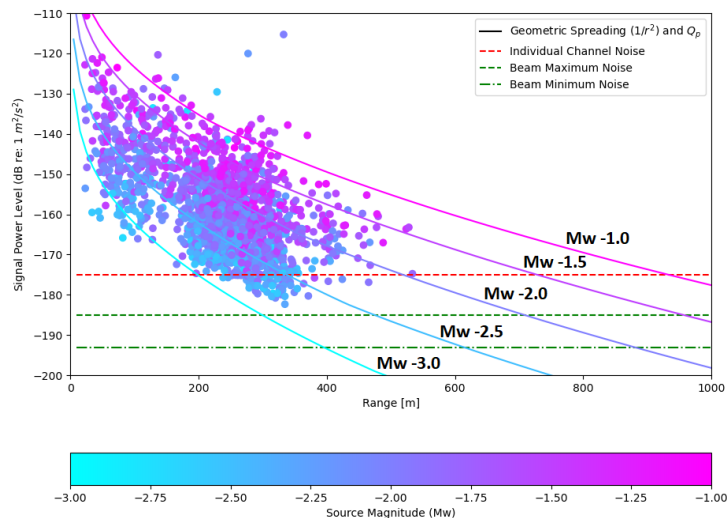


Figure 8. Received peak signal power vs. source-receiver range for 412 well-located events color coded by moment magnitude Mw from November 2021 through October 2023. Catalog events were filtered for supportable depths $z > 10\text{m}$. Modeled received signal levels plotted as solid lines include propagation losses. Time domain measured noise estimates are superimposed (red dashed line); the low-noise levels are calculated using measured array gains of $\sim 10\text{ dB}$ (green dashed line) and $\sim 18\text{ dB}$ (dot-dash line) applied to the plotted measured noise level.

The fused measured event, noise, and model information shown in Figure 8 suggests that for events with $M_w \leq -2.5$, reliable detection and high confidence location and depth is limited to a maximum source receiver range of ~ 600 meters for events occurring during minimum noise levels or just above 450 meters for maximum noise levels, requiring a signal excess peak power of $SE \geq \sim 10\text{ dB}$. If we relax the confidence restrictions, the received signal model suggests that a -3 Mw may be detectable and locatable at 400 m for overnight noise levels corresponding to the maximum array gain estimate, and at 200 m using single sensors from the SADAR arrays at mid-day noise levels. However, based on this analysis, it is doubtful that surface sensors would be able to detect, locate, and resolve the depth of -3 Mw events and smaller at the depth of the BBRS reservoir when considering noise levels measured with the surface sensor cluster. Finally, the received signal vs range considerations indicate the magnitude of completeness M_c for the SADAR system bulletin of locatable microseismic events within network should not be smaller than about -2.5 Mw.

Discussion and Conclusions

Over the past three years, the sparse network of four permanent SADAR compact volumetric phased arrays that Quantum installed in November 2021 at the CMC Newell County FRS has demonstrated a robust capability for continuous passive monitoring of microseismic events for GCS facilities. The SADAR systems and sparse network approach for persistent reliable

monitoring is designed for general industrial seismic monitoring where surveillance of geologic assets is important for risk management. Furthermore, the GCS continuous monitoring effort has allowed formulation and validation of a system performance model, with performance prediction tied to monitoring requirements, local geology, earth model, and geophysical state. Measuring the performance of the SADAR array network and processing pipeline systems for continuous MMV is now an ongoing task; completing and validating the performance model such that it can be used to plan monitoring system deployments for other sites and applications and for verifying system effectiveness is a priority.

The three year-long continuous seismic signal collection allows assessment of the factors identified in the original performance model. Measurements indicate that coherent processing of the data acquired using SADAR arrays provide noise level suppression from 10dB to ~18dB over individual channels (Zhang *et al.*, 2023), and measured noise suppression of beamformed SADAR arrays over the individual surface nodes at the FRS is at least ~30dB (Nyffenegger *et al.*, 2023). This study also reports 10 dB and 24 dB gains measured across the band for the beamformed SADAR arrays compared to the single elements and beamformed surface nodal array (respectively).

When combined with the extension of the mathematical framework to include standard seismic source models, and the algorithm implementation for generating a prediction across the network, the continuous data record allows an imperfect validation of the model. We consider the validation adequate but imperfect because the data scarcity and distribution of microseismic events away from the injection well precludes support in the majority of grid cells of the model grid. Nevertheless, the central core of the model extending beyond the industrial complex and to depths including the reservoir is well sampled and provides excellent agreement. The ongoing FRS seismic bulletin including events in the range $M_w = [-2.75, \dots, -0.9]$ provides confidence that the predictions are reasonable. The SADAR sparse network is predicted effective down to $M_c = -2.5$ M_w across the active part of the BBRS reservoir, but validation data does not provide support down to the operating BBRS reservoir across the entire area of review. This estimate of the magnitude of completeness matches the estimate of M_c for the FRS seismic bulletin. The coverage varies for deeper reservoirs and at the extremes of the network coverage such that $M_c = -2.0$ is a more conservative estimate for deeper horizons and approaching the network perimeter. The performance prediction maps (e.g., Figure 6) and the measured received signal power vs. range (e.g., Figure 8) suggest that the lack of validation data covering many of the grid cells is the actual physical condition and not a sampling or detection issue. Periodically executing the model validation allows assessing ongoing monitoring network effectiveness as the seismic bulletin is updated adding additional events.

Taken together, the performance prediction, validation data maps, and power versus range graph indicates the system parameters that control beamforming, detection, and location yield a total system performance within expectations. This method allows for *a-priori* performance prediction, requiring only limited knowledge of the earth model, the measured surface noise, and the configuration/location of arrays within the network. The model may then be periodically validated

against a continuously produced seismic bulletin. The model is therefore valuable as a planning tool, and then also as confirmation the network and processing system is performing up to expectations when compared with a local event bulletin.

Acknowledgements

Quantum Technology Sciences, Inc., is a wholly owned subsidiary of Geospace Technologies Corporation, Inc. We acknowledge CMC for providing access to the Newell County Facility to enable installation of the SADAR system, and for sharing the data from the surface and downhole networks. The Newell County Facility is supported by funding from the Global Research Initiative at the University of Calgary from the Canada First Research Excellence Fund and from the CaMI Joint Industry Project. CMC is also acknowledged for providing operational data from the site.

References

- Aki, K., and P.G. Richards, 2002, *Quantitative Seismology. Theory and Methods*. Freeman, San Francisco.
- Abraham, D.A., 2019, *Underwater Acoustic Signal Processing*. Springer Nature Switzerland, Cham.
- Ainslie, M.A., 2010, *Principles of Sonar Performance Modeling*. Springer-Verlag, Berlin.
- Bauer, R.A., Will, R., El-Kaseeh, G., Jaques, P., Greenberg, S., and Carney, M., 2022, Microseismic monitoring, event location, and focal mechanisms at the Illinois Basin-Decatur Project, Decatur, Illinois, USA. *in* *Geophysical Monitoring for Geologic Carbon Storage*, Geophysical Monograph 272, edited by Lianjie Huang, John Wiley & Sons, Inc., Hoboken. DOI: 10.1002/9781119156871.ch19.
- Boatwright, J. and Choy, G.L., 1986, Teleseismic estimates of the energy radiated by shallow earthquakes. *Journal of Geophysical Research*, **91**, pp. 2095-2112.
- Boatwright, J., Choy, G.L., and Seekins, L.C., 2002, Regional estimates of radiated seismic energy. *Bulletin of the Seismological Society of America*, **92**, pp. 1241-1255.
- Brune, J., 1971, Correction. *Journal of Geophysical Research*, **75**, 5002.
- Brune, J.N., 1970, Tectonic stress and the spectra of seismic shear waves from earthquakes. *Journal of Geophysical Research*, **75**, 4997-5009.
- Buchanan, R.C., Young, M.H., and Murray, K.E., 2023, Recent seismicity in the southern midcontinent, USA: scientific, regulatory, and industry responses. *The Geological Society of America Special Paper 559*, Geological Society of America, Boulder.
- Burdic, W.S., 1991, *Underwater Acoustics System Analysis, Second Edition*, Prentice-Hall, Englewood Cliffs.
- Choy, G.L., J.L. Boatwright, and S. Kirby, 2001, The radiated seismic energy and apparent stress of interplate and intraplate earthquakes at subduction zone environments: implications for seismic hazard estimation. USGS Open File Report 01-0005, U.S. Geological Survey.
- Dichiarante, A.M., Langet, N., Bauer, R.A., Goertz-Allmann, B.P., Williams-Stroud, S.C. Kühn D., Oye, V., Greenberg, S.E., Dando, B.D.E., 2021, Identifying geological structures through microseismic cluster and burst analyses complementing active seismic interpretation. *Tectonophysics*, **820**, 229107. DOI: 10.1016/j.tecto.2021.229107
- Eaton, D.W., 2018, *Passive seismic monitoring of induced seismicity*. Cambridge University Press, New York, NY. <https://doi.org/10.1017/9781316535547>
- Fang, X., Chen, T., Li, S., Brooks, N., Knap, G. Huffman, A.R., Lupo, T., and Storniolo, R., 2024, Evaluating the effects of velocity models and array configuration on induced seismic event locations in the Permian Basin. *Geophysics*, **89**, L1-L20.
- Hutchenson, K.D., Jennings, J., Grant, E.B., Quigley, D., Yelton, J., Nyffenegger, P.A., 2025, Persistent microseismic monitoring using robust permanent SADAR arrays. To be presented at Carbon Capture, Utilization, and Storage conference (CCUS) 2025, March 3-5, Houston TX.

- Hutchenson, K.D., D. Quigley, J. Longbow, E.B. Grant, P.A. Nyffenegger, J. Jennings, M.A. Tinker, M. Dahl, D. Grindell, M. Macquet, and D.C. Lawton, 2023, Microseismic monitoring using SADAR arrays at the Newell County carbon storage facility: what have we learned in a year? presented at Geoconvention, 2023, Calgary.
- Keilis-Borok, V.I., 1959, On the estimation of the displacement in an earthquake source and of source dimensions. *Annali di Geofisica*, **12**, 205 – 214.
- Lawton, D.C., Dongas, J., Osadetz, K., Saeedfar, A., and Macquet, M., 2019, Chapter 16: Development and analysis of a geostatic model for shallow CO₂ injection at the Field Research Station, Southern Alberta, Canada. *in* T. Davis, M. Landro, and M. Wilson, eds., *Geophysics and Geosequestration*: Cambridge University Press, 280-296, doi.org/10.1017/9781316480724.017.
- Macquet, M., Lawton, D., Osadetz, K., Maidment, G., Bertram, M., Hall, K., Kolkman-Quinn, B., Monsegny Parra, J., Race, F., Savard, G., and Wang, Y., 2022, Overview of Carbon Management Canada's pilot-scale CO₂ injection site for developing and testing monitoring technologies for carbon capture and storage, and methane detection. *Recorder Focus Article*, **47**(1), April 2022.
- Macquet, M. and D. Lawton, 2019, Exploring continuous seismic data for monitoring CO₂ injection at the CaMI Field Research Station, Alberta, Canada. SEG 89th Annual Meeting, pp 4913-4917.
- Nyffenegger, P.A., Lawton, D.C., Macquet, M., Quigley, D., Kolkman-Quinn, B., and Hutchenson, K.D., 2025, Advances in coupled passive and active seismic monitoring for large-scale geologic carbon storage projects. *in* Wilson, M., T. Davis, and M. Landro, eds., *Geophysics and the Energy Transition*: Elsevier Press, 333-354.
- Nyffenegger, P.A., Zhang, J., Grant, E.B., Quigley, D., Hutchenson, K.D., Tinker, M.A., Lawton, D.C., and Macquet, M., 2023a, Performance and outlook for SADAR array network at the Newell County Facility. *First Break*, **41**, 56-62.
- Nyffenegger, P.A., Grant, E.G., Zhang, J., Jennings, J., Quigley, D., Hutchenson, K.D., Tinker, M.A., Macquet, M., and Lawton, D.C., 2023b, Estimates of performance model factors for passive microseismic SADAR phased arrays at the Newell County Facility. *GeoConvention, Conference Abstracts*. <https://geoconvention.com/wp-content/uploads/abstracts/2023/91418-estimates-of-performance-model-fac.pdf>
- Quigley, D., Nyffenegger, P. A., Hutchenson, K.D., Yelton, J., 2025, Active source sparse imaging using permanent SADAR arrays. To be presented at Carbon Capture, Utilization, and Storage conference (CCUS) 2025, March 3-5, Houston TX.
- Roux, P.R., Kostadinovic, J., Bardainne, T., Rebel, E., Chmiel, M., Van Parys, M., Macault, R., and Pignot, L., 2014, Increasing the accuracy of microseismic monitoring using surface patch arrays and a novel processing approach. *First Break*, **32**, 7, 95-101 <https://doi.org/10.3997/1365-2397.32.7.76891>
- Stork, A.L., Verdon, J.P., J.M. Kendall, 2015, The microseismic response at the InSalah carbon capture and storage (ccs) site. *International Journal of Greenhouse Gas Control*, 159-171. <http://dx.doi.org/10.1016/j.ijggc.2014.11.014>
- Urlick, Robert J., 1983, *Principles of Underwater Sound*, 3rd Edition. Peninsula Publishing, Westport.
- Zhang, J., Hutchenson, K.D., Nyffenegger, P.A., Grant, E.B., Jennings, J., Tinker, M., Macquet, M. and Lawton, D.C., 2023. Performance comparison of compact phased arrays and traditional seismic networks for microseismic monitoring at a CO₂ sequestration test site. *The Leading Edge*, **42**(5), 332-342.